Astron. Astrophys. 353, 371–379 (2000)

ASTRONOMY AND ASTROPHYSICS

Optical CCD imaging of the supernova remnant CTA 1

F. Mavromatakis[1], **J. Papamastorakis**[1,2], **E.V. Paleologou**[2], **and J. Ventura**[1,2]

[1] University of Crete, Physics Department, P.O. Box 2208, 710 03 Heraklion, Crete, Greece
[2] Foundation for Research and Technology-Hellas, P.O. Box 1527, 711 10 Heraklion, Crete, Greece

Received 2 June 1999 / Accepted 26 October 1999

Abstract. Deep Hα + [NII], [NII], [SII] and [OIII] CCD images have been obtained from the high galactic latitude supernova remnant CTA 1. The filamentary morphology in the light of the [OIII] emission is now clearly seen in the full field of the remnant. Contrary to the [OIII] morphology, the remnant appears less sharply defined in the light of the Hα + [NII], [NII] and [SII]. The morphological differences between the [OIII] and Hα + [NII] emission lines and the presence of a number of filaments with projected lengths ranging from 0.5 to several pc suggest an inhomogeneous insterstellar medium. The presence of incomplete recombination zones is supported by the variations seen in the [OIII]/H$_\beta$ ratio which ranges from 5–20. A low dispersion spectrum taken in the south of CTA 1 indicates surface brightness values of Hα, [NII] and [SII] of $\sim$ 13, 14 and 18 in units of 10^{-17} erg s^{-1} cm^{-2} arcsec^{-2} respectively, while the sulfur line ratio suggests an electron density of $\sim 200\,\mathrm{cm}^{-3}$. Rough upper limits to the preshock cloud density are of the order of ~ 1 nuclei cm^{-3}. The strong [OIII] emission is indicative of shock velocities higher than 100 km s^{-1} while in certain areas of the remnant where the Hα emission dominates lower velocities are possible. It is the first time that significant optical emission is detected in the northwest area of the remnant, where diffuse radio emission is mainly seen. The small scale filaments detected there and their flux suggest that we observe shocked material, most likely associated to CTA 1. Three more distinct filamentary structures are detected in the south-west area, outside of the main emission shell. Their lengths range from $1\farcm5$ to $6\farcm5$. The spatial locations of the newly detected emission features suggest an angular shock radius of $59'$.

Key words: book reviews – ISM: supernova remnants – ISM: individual objects: CTA 1

1. Introduction

The galactic supernova remnant CTA 1 (G119.5+10.2) displays a shell-like morphology, although not complete, in radio wavelengths (Pineault et al. 1997) and a center-filled morphology at X-ray wavelengths (Slane et al. 1997) while observations in the 5007 Å line of [OIII] show that the optical morphology resembles that of the radio (Fesen et al. 1981, Fesen et al. 1983). Pineault et al. (1993) using HI data proposed that the remnant lies at a kinematic distance of 1.4 kpc. Extended radio observations have been presented by Pineault et al. (1993, 1997) together with a breakout model for CTA 1. According to this model, the main shock front in the north-west suddenly passed from a medium of typical interstellar density to a medium of much lower density. The diffuse nature of the radio emission and the steepening of the radio spectrum is attributed to the breakout by the authors. Furthermore, the radio images of CTA 1 display several interesting features, like the central emission bridge, the "reverse shell", the hook feature etc. using the terminology of Pineault et al. (1997). The X-ray emission is basically confined by the outer radio contours, being brightest at the center of the remnant and decreasing towards the periphery (Slane et al. 1997). They also showed that the spectra taken by ROSAT and ASCA could not be fit by a single model. A composite model consisting of a thermal and non-thermal component could fit the data. The non-thermal component dominates the emission in the central area of the remnant and is attributed by these authors to a strong synchrotron nebula powered by an, as yet, unseen pulsar. The thermal component dominates in the outer parts of the remnant and is associated with the propagation of the shock front into the interstellar medium (ISM) of relatively low density (Slane et al. 1997). The ISM densities derived from X-ray data based on the Sedov solution are, in general, lower than those derived from optical measurements while the inverse holds for the shock velocities. This is because the optical and X-ray emission outline different regions of the remnant. The X-ray emission probes the hot gas (T $\sim 10^6$ K) resulting from the interaction of the blast wave and the ISM, while the optical emission arises from secondary shocks in dense clouds found in an inhomogeneous ISM. The induced shock travels through the clouds at a lower speed (80–200 km s^{-1}) than the X-ray shock and the cooling of matter behind it gives rise to the observed optical emission (e.g. McKee et al. 1975, Blandford & Cowie 1982, White & Long 1991). The [OIII] line emission is produced closer to the shock front than the radiation from Hα, [NII] and [SII]. The latter lines are believed to originate from cooler regions further away from the shock front (Cox 1972). The low ionization lines are thus mostly affected by density variations

Send offprint requests to: F. Mavromatakis (fotis@physics.uch.gr)

Table 1. Interference filter characteristics

Filter	Wavelength[a] (FWHM)(Å)	Line (%) contributions
Hα +[NII]	6555 (75)	100, 100, 100[b]
[NII]	6577 (20)	3.5, 41, 100[b]
[SII]	6708 (27)	100, 18[c]
[OIII]	5005 (28)	100
Cont red	6096 (134)	–
Cont blue	5470 (230)	–

[a] Wavelength at peak transmission for $f/3.2$
[b] Contributions from λ6548, 6563, 6584 Å
[c] Contributions from λ6716, 6731 Å

and inhomogeneities of the preshock interstellar medium (Hester 1987).

CTA 1 is visible with difficulty on the red Palomar survey plates but appears quite strong when imaged in the line of [OIII] λ5007 Å. Fesen et al. (1981), using interference filters, obtained low resolution (30′′ - 40′′) wide field photographic plates showing the full extent of the remnant in [OIII] but they did not reproduce the Hα + [NII] and [SII] images because they were too faint. Subsequent, higher resolution photographs by Fesen et al. (1983) in restricted fields revealed the filamentary nature of the oxygen emission.

In this work we present the first CCD images of CTA 1 in main optical emission lines, covering a wide field of $2^\circ \times 2^\circ$ at a scale of 4′′ per pixel. The new optical images show intricate filamentary and diffuse structures, and allow a comparison with earlier radio and X-ray observations. The details revealed here demonstrate the advantage of CCD imaging which, coupled to the wide field of view, allows the exploration of faint extended objects. Information concerning the observations and data reduction is given in Sect. 2, while in Sect. 3 we present the morphology of the remnant in the different filters used to image CTA 1. In addition, flux measurements based on the spectrum and the image calibration are given. Finally, in Sect. 4 the overall properties of the remnant and the interstellar medium are discussed.

2. Observations

2.1. Optical images

The optical images of CTA 1 were obtained with the 0.3 m telescope at Skinakas Observatory from August 21 to August 24, 1998. The focal ratio of 3.2 of the Schmidt Cassegrain telescope together with the 1024 × 1024 Thomson CCD resulted in a $69' \times 69'$ field of view and a $4''.12$ pixel^{-1} image scale. Given the large physical extent of the remnant, we observed the south-west ($\alpha \simeq 23^{\rm h}59^{\rm m}$, $\delta \simeq 72^\circ 20'$), southeast ($\alpha \simeq 00^{\rm h}11^{\rm m}$, $\delta \simeq 72^\circ 20'$), northeast ($\alpha \simeq 00^{\rm h}11^{\rm m}$, $\delta \simeq 73^\circ 20'$) and northwest ($\alpha \simeq 23^{\rm h}59^{\rm m}$, $\delta \simeq 73^\circ 20'$) fields in each of the filters listed in Table 1. All coordinates in this work refer to epoch 2000. Each field was observed for 1800 s at two separate instances, i.e. the total exposure time is 3600 s while the overlapping areas have an effective exposure time of 7200 s. Due to the large spatial size of CTA 1, individual fields represent specific projections of the sky onto the plane of the CCD camera. These fields must be mapped to a common projection before any image combination is performed. An astrometric solution was calculated for every field and every filter using stars from the Hubble Space Telescope Guide Star catalogue.

Standard IRAF and MIDAS routines were used for the reduction of the data. Individual frames were bias subtracted and flat-field corrected using twilight flat-fields. The spectrophotometric standard stars HR7596, HR7950, HR8634, and HR718 were used for flux calibration.

2.2. Optical spectrum

A low dispersion spectrum was obtained on August 21, 1998 using the 1.3 m telescope at Skinakas Observatory. The data were taken with a 1300 line mm^{-1} grating and a 1024 × 1024 Tektronix CCD having a 24 μm pixel size which resulted in a 1.68 Å pixel^{-1}. The slit had a width of 3′′.3 and was sufficiently long to allow good sky background determination. It was centered at α = $00^{\rm h}09^{\rm m}15^{\rm s}$, $\delta = 72^\circ 14' 15''$and oriented in the south-north direction. The exposure time was 1800 s. The spectrum, covering the range of 5510–7180 Å, was reduced using standard IRAF procedures and the spectrophotometric standard stars HR7596, HR7950, HR8634 for flux calibration.

3. Results

3.1. The [OIII] *line emission*

The emission from the [OIII] λ5007 Å forbidden line of oxygen is presented in Fig. 1. Visible in the [OIII] image are limb-brightened filaments in the south, south-west area of CTA 1 while the emission weakens and becomes more diffuse in the north, north-east area. Bright arcs and diffuse emission in [OIII] are seen at positions I, II, III and IV (see Fig. 1). The arc at position I has a length of $\sim 12'$ while that at position II extends for $\sim 11'$. The diffuse emission at position III has an extent of $\sim 17'$ and the length of the faint emission at position IV is $\sim 10'$. The emission seen at positions III and IV is found in the area of the "reverse shell" as termed by Pineault et al. (1997). As we move to the north-east, we run across a significant reduction in flux, by a factor of ~ 2, around $\alpha \simeq 00^{\rm h}15^{\rm m}$and between δ $72^\circ 45'$and $\delta \simeq 73^\circ 00'$. However, after $\delta \simeq 73^\circ 00'$the oxygen line intensity returns to the level before the gap but seems to split into two filaments with a maximum separation of $\sim 2'$. These join smoothly at $\alpha \simeq 00^{\rm h}13^{\rm m}.5$, $\delta \simeq 73^\circ 11'$. Note, that the filament after the gap surrounded by the diffuse emission may be the physical extension of the filament located before the gap, running from $\delta \simeq 72^\circ 32'$ to $\delta \simeq 72^\circ 45'$ along $\alpha \simeq 00^{\rm h}16^{\rm m}$. We emphasise that the drop in intensity in the gap cannot be an artifact of the data since this part of the image has an effective exposure time of 7200 s, being present in both the south-east and north-east fields. Furthermore, this gap is also present in the images of Hα + [NII] (Fig. 2), and [SII] (Fig. 3). East of the above two filaments in the north, there is a patch of faint, diffuse

emission with a diameter of $\sim 15'$. Faint emission is seen even further north, past $\delta \simeq 73^\circ 30'$.

In the interior of CTA 1, we see that the emission is mainly faint and diffuse. However, there are some filamentary structures. One is located at $\alpha \simeq 00^{\rm h}10^{\rm m}30^{\rm s}$, $\delta \simeq 72^\circ 28'$ with a length of $\sim 5'$ and one emerging from the south boundary at $\alpha \simeq 00^{\rm h}05^{\rm m}12^{\rm s}$, $\delta \simeq 72^\circ 08' 30''$ extending directly to the north for $\sim 5'$, continuing after a gap of $\sim 9'$ for another $\sim 6'$ before merging to the diffuse nebulosity at $\alpha \simeq 00^{\rm h}05^{\rm m}$, $\delta \simeq 72^\circ 30'$. Additionally, diffuse emission is marginally present between $\delta \simeq 73^\circ 17'$ and $\delta \simeq 73^\circ 33'$at $\alpha \simeq 00^{\rm h}02^{\rm m}$.

3.2. The Hα + [NII] *and* [SII] *emissions*

The [OIII] image (Fig. 1) is markedly different from the Hα + [NII] (Fig. 2), and [SII] (Fig. 3) images, especially in the south, south-west perimeter of the remnant. The Hα + [NII] emission along the southern rim is mainly diffuse, although filamentary emission is seen in position I and also $\sim 10'$ away to the north west from this position, spatially correlated with an oxygen filament. However, the extent of the Hα+[NII] emission at position I is roughly $\sim 8'$ less than that seen in the [OIII] image. Especially, in this part of the remnant there are striking differences between the Hα + [NII] and [OIII] morphologies. A close-up of this area is shown in Fig. 4 and Fig. 5.

The bright emission in [OIII] at $\alpha \simeq 00^{\rm h}05^{\rm m}$, $\delta \simeq 72^\circ 07'$ is not as prominent as in Hα + [NII] while there is only partial overlapping between oxygen and Hα + [NII] emission around $\alpha \simeq 00^{\rm h}09^{\rm m}$, $\delta \simeq 72^\circ 10'$. A bright emission knot in Hα + [NII] is not present in the [OIII] image. Further to the north–east, we see that the flux discontinuity (the gap) is also present in the Hα + [NII] image as well as in the [SII] image. However, the length of the gap is longer here and Hα + [NII] emission shows up again after $\sim 20'$. The morphology of the emission after the gap is filamentary and partially correlated with the [OIII] emission. The part of the emission at almost constant declination ($\delta \simeq 73^\circ 12'$), from $\alpha \simeq 00^{\rm h}12^{\rm m}50^{\rm s}$ to $\alpha \simeq 00^{\rm h}11^{\rm m}10^{\rm s}$ has no counterpart in the [OIII] image. No filamentary emission is detected further to the north of $\delta \simeq 73^\circ 12'$ and further to the east of $\alpha \simeq 00^{\rm h}15^{\rm m}$. The hook feature and the central emission bridge feature observed in the radio morphology (Pineault et al. 1997) are not detected in the optical images. However, there is faint Hα emission connecting $\alpha \sim 00^{\rm h}06^{\rm m}$, $\delta \sim 72^\circ 40'$ and $\alpha \sim 00^{\rm h}12^{\rm m}$, $\delta \sim 73^\circ 14'$.

The interior emission morphologies are similar to those of the [OIII] emission. Faint and filamentary emission is also seen around $\alpha \simeq 00^{\rm h}10^{\rm m}30^{\rm s}$, $\delta \simeq 72^\circ 28'$, at the same position where a filament of $\sim 6'$ length is seen in [OIII]. The emission along $\alpha \simeq 00^{\rm h}02^{\rm m}$ from $\delta \simeq 73^\circ 17'$ to $\delta \simeq 73^\circ 33'$ is also present in Hα + [NII] but appears more prominent and filamentary than in the [OIII] image. Additionaly, there are a few filamentary structures at $\alpha \simeq 23^{\rm h}55^{\rm m}$, $\delta \simeq 73^\circ 17'$, located in the "breakout" area postulated by Pineault et al. (1997), which is seen also in [SII] while it is much fainter in [OIII]. Three more filaments are detected in the south-west region, the first is located at $\alpha \simeq 23^{\rm h}53^{\rm m}$, $\delta \simeq 72^\circ 39'$ with a length $\sim 6\farcm5$, the second at $\alpha \simeq 23^{\rm h}51^{\rm m}30^{\rm s}$, $\delta \simeq 72^\circ 39' 19''$ with a length of $1\farcm5$ and the third at $\alpha \simeq 23^{\rm h}53^{\rm m}40^{\rm s}$, $\delta \simeq 72^\circ 22' 31''$ with a length of $\sim 4'$. The positions of the first and third filament are marked by the arrows shown in Fig. 2. The second filament is only $6'$ away to the west of the first. The projected thicknesses of these filaments range from $10''$ to $35''$.

Table 2. Optical spectrum fluxes

Wavelength (Å)	$F^{a,b}(\lambda)$	$I^{b,c}(\lambda)$	$F^{d}_{H\alpha}$
6548 [NII]	3.5	2.2	27.6
6563 Hα	12.7	7.9	100
6584 [NII]	10.5	6.6	82.7
6716 [SII]	10.1	6.1	79.5

[a] Uncorrected for interstellar extinction
[b] in units of 10^{-17} erg s^{-1} cm^{-2} arcsec^{-2}
[c] Corrected for interstellar extinction ($c = 0.62$)
[d] Fluxes normalized to F(Hα)=100

3.3. The optical spectrum and flux estimates

In Table 2, we list the observed fluxes from the low dispersion spectrum centered at the bright feature at α = $00^{\rm h}09^{\rm m}15^{\rm s}$, δ = $72^\circ 14' 15''$. The slit position and orientation are shown in Fig. 2. Source counts were added along the slit in order to maximize the signal to noise. Typical error on the quoted fluxes is $\pm$2.4 in units of 10^{-17} erg s^{-1} cm^{-2} arcsec^{-2}. The ratio of the sulfur lines [SII] $\lambda\lambda$6716, 6731 allow us to determine the electron density n_e at the observed position (e.g. Osterbrock 1989). Because the two lines are very close and in the absence of an independent determination of the interstellar extinction, the uncorrected fluxes are used to estimate a filament electron density of 200 cm^{-3} (Shaw et al. 1995). The sulfur line ratio has an error of $\sim$25% (1.23$\pm$0.30) which translates into a large uncertainty in the determination of the electron density. Formally, only an upper limit of 900 cm^{-3} can be set to the electron density. However, the correct value of electron density may lie in the range of $\sim$100–200 cm^{-3} since the spectrum obtained by Fesen et al. (1981) also suggests a similar electron density. Published data on the neutral hydrogen column density are used to estimate the interstellar extinction, c. Slane et al. (1997) obtained a column density of $2.8(\pm0.5) \times 10^{21}$ cm^{-2} from ROSAT and ASCA data of CTA 1. Assuming that N_H = $6.8(\pm1.6) \times 10^{21}$ cm^{-2} mag^{-1} $\times$ E(B-V) (Ryter et al. 1975), we obtain a color excess of 0.412 ± 0.120 mag. The algorithm of Hakkila et al. (1997), based on previously published studies of the insterstellar extinction, is also utilised. Setting l = 119°.5 and b = 10°.2 for the galactic position of CTA 1 and adopting a distance of 1.4 kpc, we obtain $A_v = 1.27 \pm 0.41$, corresponding to E(B-V) = 0.41 ± 0.13 mag ($A_v = 3.1 \times$ E(B-V)). The weighted average of the above values is 0.41 ± 0.09 mag, equivalent to c = 0.62 ± 0.14. The interstellar reddening curve of Whitford (1958) as presented by Kaler (1976) was used for the calculation above.

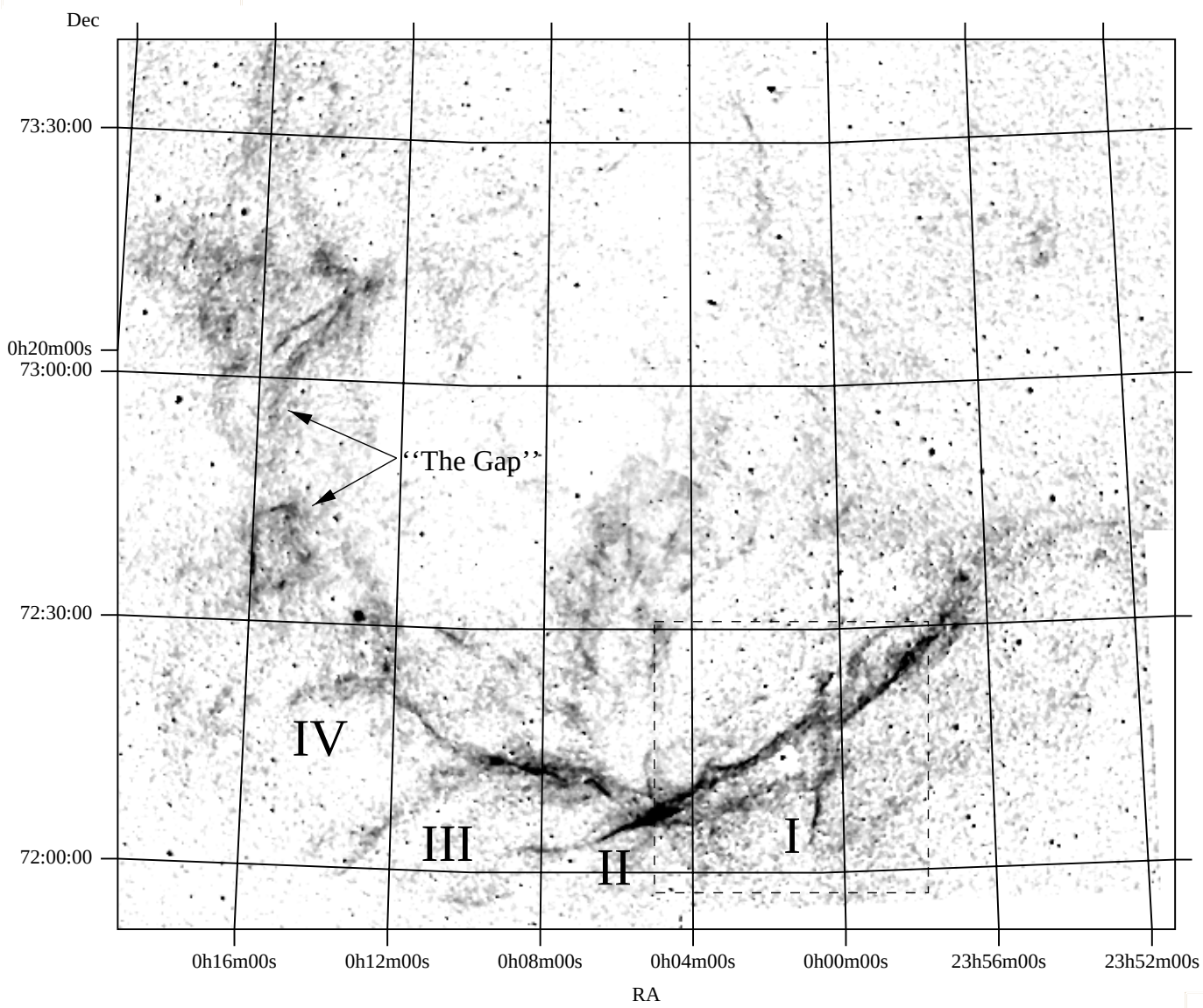

Fig. 1. CTA 1 imaged in the [OIII] λ5007 Å emission line. The image has been smoothed to suppress the residuals from the imperfect continuum subtraction. North is up, east to the left and the coordinates refer to epoch 2000. Shadings run linearly from 0.0 to 10×10^{-17} erg s^{-1} cm^{-2} arcsec^{-2}. The dashed box indicates the area shown in Fig. 4 and Fig. 5.

Typical surface brightness values of CTA 1 in Hα + [NII], [NII], [SII] and [OIII] are 20.0, 7.0, 7.5, 12.0 (5–10σ confidence) respectively, in units of 10^{-17} erg s^{-1} cm^{-2} arcsec^{-2}. These values are not corrected for interstellar extinction. Denoting by f_n the flux ratio of the [NII] image over the Hα + [NII] image, by f_s the ratio of the [SII] image over the Hα + [NII] image, and by f_o the ratio of the [OIII] image over the Hα + [NII] image, we find that f_n = 0.51±0.05 and f_s = 0.40±0.05 over regions of the remnant where meaningful estimates can be obtained. The f_o ratio is ~ 0.5 at bright Hα + [NII] areas while at bright [OIII] regions exceeds unity. Both the f_s and f_o quoted values are actually lower limits to the intrinsic ratios since the denominator includes the contribution from both nitrogen lines at 6548 Å and 6584 Å. Correcting for this with the help of the spectrum, and assuming I(Hα)/I(Hβ) = 3.0, and c = 0.62, we obtain [SII]/H$\alpha > 0.8$, [OIII]/H$\beta \sim 5$ at bright Hα + [NII] regions and [OIII]/H$\beta \sim$ 10–20 at bright [OIII] regions. The sulfur to Hα ratio suggests that we are observing shocked material (e.g. Fesen & Hurford 1995) while the oxygen to Hβ ratio suggests the presence of numerous incomplete recombination zones (Raymond et al. 1988).

4. Discussion

The morphology of CTA 1 is both filamentary and diffuse. It is mainly filamentary in the light of [OIII] while the filaments in Hα and [SII] are less well defined. The different morphologies are believed to be the result of different perspectives. Edge-on view of a thin–sheet–like shock front will result in a sharper filamentary appearance while face-on view will result in a diffuse appearance (Hester 1987). It is clear that in the former case

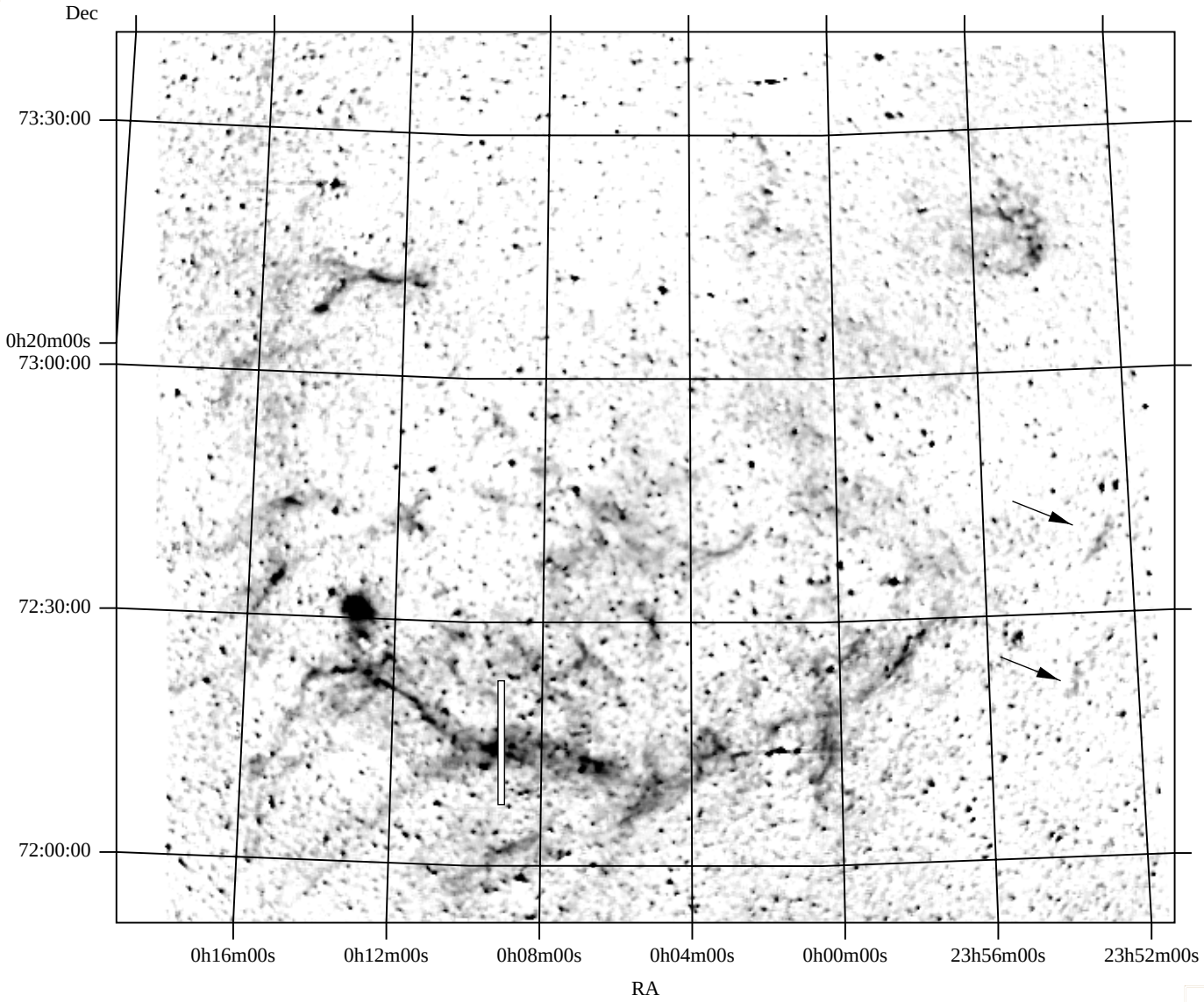

Fig. 2. CTA 1 imaged with the Hα+[NII] filter. The image has been smoothed to suppress the residuals from the imperfect continuum subtraction. North is up, east to the left and the coordinates refer to epoch 2000. The thick white line shows the slit position and the arrows indicate the positions of the newly detected filamentary structures. Shadings run linearly from 0.0 to 14 $\times$ 10^{-17} erg s^{-1} cm^{-2} arcsec^{-2}.

we sample long lines of sight through the emitting material, while in the latter we sample much shorter lines of sight, basically through the shortest dimension of the emitting medium. The morphological differences between [OIII] and Hα suggest the presence of significant inhomogeneities in the preshock medium. The Hα emission is produced in areas of lower temperatures while the [OIII] emission is produced in areas of higher temperatures. The cooler areas are found at larger distances behind the shock front and thus, at higher column densities. Consequently, the presence of inhomogeneities would mainly affect the recombination zone where Hα is produced. Additionally, preshock density variations are expected to alter the cooling and recombination time scales, thus affecting the recombination time scales, thus affecting the recombination zone (see Hester 1987 for more details). Strong variations in the preshock density and inhomogeneities in the preshock medium must be present in the south of CTA 1, in order to explain the differences seen in Fig. 4 and Fig. 5. The morphology and the flux measurements suggest a length scale of these variations of $\sim$ 0.5 pc along the [OIII] filament.

4.1. The interstellar "clouds"

The filaments seen in [OIII] in the south perimeter of CTA 1 are characterized by a length of $\sim 20'$ and a projected thickness of $\sim 25''$ corresponding to 8 pc and 0.2 pc, respectively at a distance of 1.4 kpc. The strong [OIII] emission with respect to Hα is indicative of the presence of incomplete recombination zones where the shock has swept-up a column density of N $\simeq 10^{17.5}$ cm^{-2} (Raymond et al. 1988). A rough upper limit to

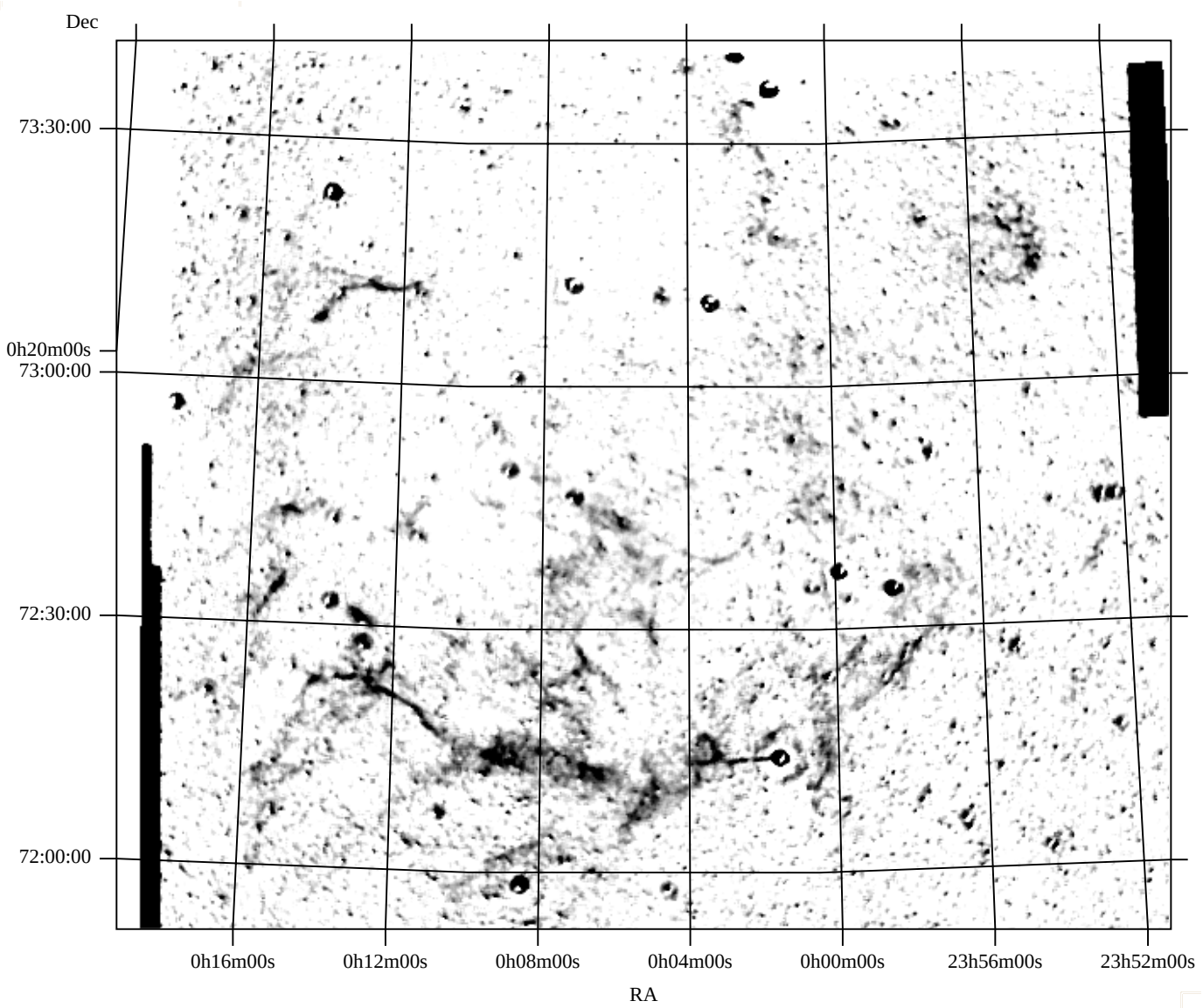

Fig. 3. CTA 1 imaged with the [SII] filter. The image has been smoothed to suppress the residuals from the imperfect continuum subtraction. North is up, east to the left and the coordinates refer to epoch 2000. Shadings run linearly from 0.0 to 5×10^{-17} erg s^{-1} cm^{-2} arcsec^{-2}.

the preshock cloud density $\mathrm{n_c}$ of ~ 0.5–$1.0\,\mathrm{cm^{-3}}$ is estimated if we assume that $\mathrm{N} = \int_0^l n(l)\,dl\ > \mathrm{n_c l}$, where l is the projected thickness of a filament (~ 0.2 pc). Another approach to the cloud density calculation involves pressure equilibrium between the shocked cloud and the shocked ISM (McKee & Cowie 1975). For a blast wave velocity $\sim 400\,\mathrm{km\,s^{-1}}$ (Slane et al. 1997) and requiring a shock velocity in the clouds of $> 100\,\mathrm{km\,s^{-1}}$ (Cox & Raymond 1985), we find that $\mathrm{n_c/n_o} < 20$, where $\mathrm{n_o}$ is the ISM density. A density $\mathrm{n_o}$ of $\sim 0.04\,\mathrm{cm^{-3}}$ (Slane et al. 1997) implies $\mathrm{n_c} < 0.8\,\mathrm{cm^{-3}}$, in agreement with the previous result. Further to the east, an electron density of $\sim\ 200\,\mathrm{cm^{-3}}$ is estimated from the low dispersion spectrum (Sect. 3.3). The presence of strong [OIII] emission at the slit position indicates a shock speed higher than $\sim$ 100–120 km s^{-1}. Using the estimated electron density $\mathrm{n_{[SII]}}$ of $\sim 200\,\mathrm{cm^{-3}}$ in the formula $\mathrm{n_{[SII]}} \simeq 45\ \mathrm{n_c} \times (\mathrm{V_s}/100\,\mathrm{km\,s^{-1}})^2$ (Fesen & Kirshner 1980, Dopita 1979) and the previous lower limit on the shock speed, we find a preshock density of $< 4\,\mathrm{cm^{-3}}$. The projected thicknesses of the filament running diagonally between positions III and IV are similar in Hα and [OIII] and the line intensities indicate the formation of a full recombination zone. For this filament, we estimate a density of $< 4\,\mathrm{cm^{-3}}$ and [OIII]/H$_\beta \sim 5$.

A bright filament in Hα + [NII] around $\alpha \simeq 00^{\mathrm{h}}11^{\mathrm{m}}$ and $\delta \simeq 73°14°$ is not detected in the [OIII] image. Assuming that this is due to a slow shock ($< 100\,\mathrm{km\,s^{-1}}$, Cox and Raymond 1985) and that pressure equilibrium holds, then we estimate a preshock cloud density of > 12 $\mathrm{n_o}$, ($\sim 0.5\,\mathrm{cm^{-3}}$). Additionally, the assumption that a full recombination zone has formed requires $\mathrm{n_c l} < 10^{18.5}\,\mathrm{cm^{-2}}$, in case of a shock with a velocity of less than $100\,\mathrm{km\,s^{-1}}$. The calculations of Raymond et al. (1988) show that the column density of a full recombination zone scales roughly as the square of the shock velocity.

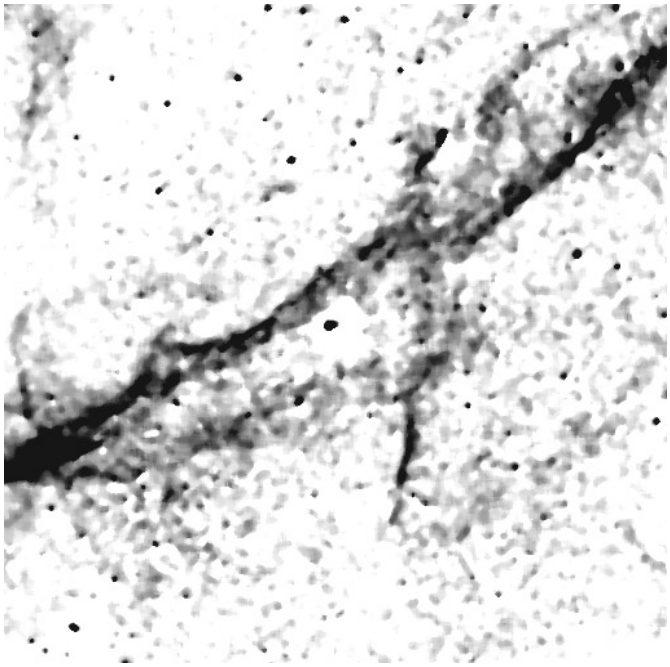

Fig. 4. CTA 1 close-up with the [OIII] filter. The center of the image corresponds to the position of the HD 224891, at α = $00^{\rm h}01^{\rm m}36^{\rm s}$and δ = $72^\circ14'12''$. North is up, east to the left and the field is $35'$ by $35'$ wide.

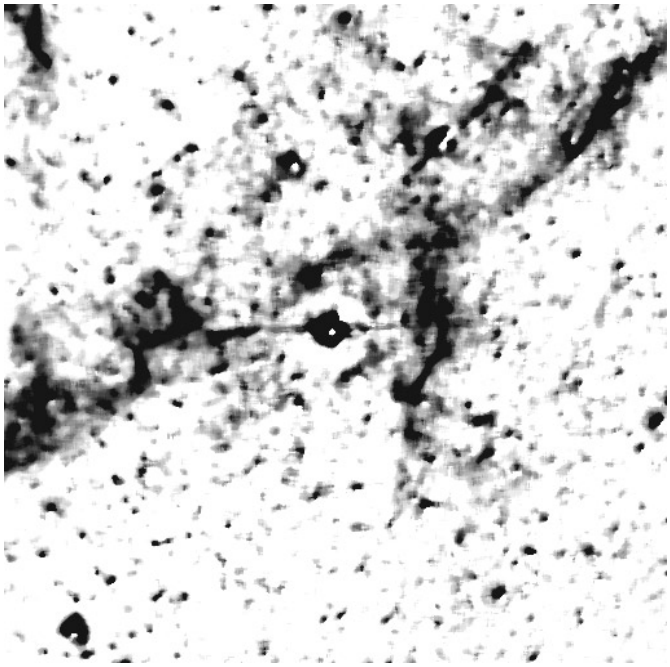

Fig. 5. The same area as in Fig. 4 imaged with the [NII] filter. Diffuse emission is mainly seen at the locations of the [OIII] filaments.

Consequently, in case of a shock with a velocity of less than 100 km s^{-1}, we expect N $< 10^{18.5}$ cm^{-2}. Given the projected thickness of $40''$ of the Hα filament, a density of < 3 cm^{-3} is found. Thus, the upper limit to the preshock cloud density is of the order of a few nuclei per cm^3.

4.2. The "reverse shell" area

Pineault et al. (1997) used the term "reverse shell" to denote a circular area (diameter $\sim 19'$) of very low radio activity in the south east area of the remnant. The authors proposed that the depression seen in the radio emission maps results from the interaction of a very dense cloud and the supernova blast wave.

We note that the depression fits between the two filamentary arms marked III and IV (see Fig. 1, Fig. 6) while the Hα + [NII] emission, at the same positions, extends even further out from the main shell of optical emission. Especially, the emission at position III falls within the circle of diameter $19'$ centered at $\alpha \simeq 00^{\rm h}12^{\rm m}.5$, $\delta \simeq 72^\circ10'$. In order to examine in more detail the conditions in this area, we have retrieved archival IRAS data at 60 μm and radio data at 4850 MHz from the High Energy Astrophysics Science Archive Research Center. The retrieved IRAS image has been processed by the Infrared Processing and Analysis Center (IPAC) and is characterized by a resolution of $\sim 2'$ (Wheelock et al. 1994) while the radio image was taken from the Green Bank survey (Condon et al. 1994) and is characterized by a FWHM of $\sim 3\farcm5$. Contours of the [OIII], infrared and radio emission of the "reverse shell" area are shown in Fig. 6 as solid, dashed and dash-double dotted lines, respectively. This figure shows that the optical and radio data are rather well correlated at positions III and IV and that the optical data are anti-correlated with the infrared data. There is also an overlap region between the infrared and radio emission and between the infrared and the soft X-ray data (not shown here; Seward et al. 1995). However, in both cases the size of the overlapping area is $\sim 3'$– $4'$ which is comparable with the resolution of the data.

The association between the optical and radio radiation suggests a common spatial origin of these two emitting mechanisms, in which case, we can conclude that the shock must have travelled, at least, up to the outer part of the optical arc at position III, thus engulfing the dust cloud. The absence of a significant overlap between the infrared and the optical data suggests that the dust cloud is aborbing any optical radiation from the background. Assuming that the cloud density is much higher than that of the ambient medium (Pineault et al. 1997), a reflected shock is expected to form. X-ray spectra from the area before the dust cloud should be harder, due to the higher temperature, while over the dust area the X-ray flux should be reduced and more absorbed. However, the ROSAT data do not allow such analysis due to the low source count rate of $\sim 10^{-4}$ cts s^{-1} arcmin^{-2} in this part of the remnant.

4.3. The north – west area

Radiation, mainly, seen in Hα, [NII] and [SII], is detected in this area (the breakout area, Pineault et al. 1997) around $\alpha \simeq 23^{\rm h}55^{\rm m}10^{\rm s}$, $\delta \simeq 73^\circ17'00''$. A weak maximum $4'$ north of our position is reported by Pineault et al. (1993) while emission at 1720 and 2695 MHz (Sieber et al. 1981) is well correlated with the position of the optical emission. We also report that the

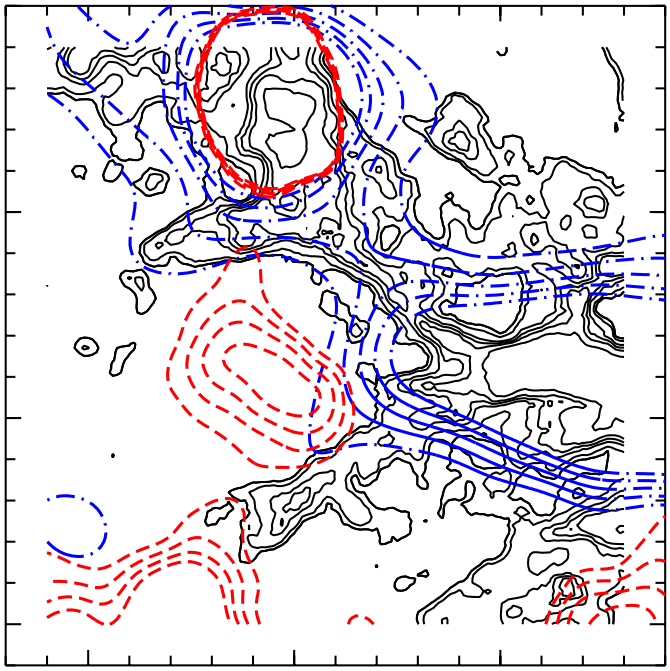

Fig. 6. The "reverse shell" imaged with the [OIII] filter (solid lines). The dashed contours represent the dust emission at 60 μ m (resolution of 2′) at values of 2.4, 2.5, 2.6, and 2.7 MJy/sr while the dash-double dotted contours represent the 4850 MHz emission (resolution of 3.′5) at values of 0.3, 0.7, 1.7, 3.4, and 6.7 K. The outer radio and optical contours are at a level of 4σ above the local background. The field is 40′ × 40′ wide and is centered at α = $00^{\rm h}12^{\rm m}.5$, δ = 72°16′. North is up, east to the left.

archived ROSAT data show extended emission (5′×5′) at exactly the same position and at a level of ∼ 1/5 of the maximum observed intensity. Eventhough the X-ray emission is located at the outer part of the PSPC detector, the presence of both optical and radio radiation, at the same spatial location, may suggest that it is a true detection and not random noise. A search in catalogues of extended objects around this position proved negative. In addition, the optical flux ratios agree rather well with those measured in other regions of the remnant. Thus, unless we are dealing with a new compact supernova remnant (12′×12′), this emission should be associated to CTA 1. The observed optical radiation is located beyond the HI and 100 μm shells, running from the southwest to the northeast (Pineault et al. 1997). The emission features seen in this area, as well as other features in the south-west (see Sect. 3.2) and south-east suggest that the shock radius may be larger than that of 50′ currently adopted. This is also supported by the extended diffuse radio emission seen at 1420 and 408 Mhz (Pineault et al. 1997). We find that a circle with an angular radius of ∼ 59′ centered at $\alpha \simeq 00^{\rm h}06^{\rm m}$ and δ ≃ 72°49′, encloses the majority of the optical emission seen in every filter. The Sedov-Taylor solution (e.g. Ostriker & McKee 1988) shows that a 18% increase in shock radius leads to an increase of E51/n_o and age of the remnant by factors of 1.2 and 1.6, respectively (E51 is the energy of the explosion in units of 10^{51} erg s^{-1}). However, a Sedov like remnant cannot produce the observed center-filled morphology. On the other hand, a physically more plausible case is that of the propagation of a shock wave into a stratified medium (e.g. Bisnovatyi-Kogan & Silich 1995, Hnatyk & Petruk 1999). Such a model, characterized by a large scale exponential distribution of the ISM density, appears to work quite well for the supernova remnant W44 and might apply also to CTA 1 (Shelton et al. 1998). In this class of problems, one more parameter is introduced, the stratification scaleheight. Adopting the analytical formulas of Maciejewski and Cox (1999), it is found that a formal solution exists for CTA 1, i.e. acceptable values of the stratification scale height, age of the remnant etc. are obtained. Typically, the stratification scale height lies in the range of 15–30 pc, the ratio E51/n_o lies in the range of 1.5–2.0, while the age of the remnant is found in the range of 23000–26000 yrs. However, detailed X-ray observations would be required to accurately determine the luminosities of the two components and the distribution of the temperature and column density over the face of the remnant, in order to test this model.

5. Conclusions

We have presented CCD images of the supernova remnant CTA 1 in the emission lines of [OIII], Hα, and [SII]. The remnant's [OIII] emission is mostly filamentary while the emission seen from Hα, [NII], and [SII] is markedly less so. Preshock density variations and inhomogeneities in the preshock ISM may be responsible for the different morphologies seen. Several incomplete recombination zones are present with estimated values of [OIII]/$H_\beta > 10$. Upper limits to the preshock density of the interstellar clouds, where the optical emission is generated, are of the order of 1 cm^{-3}, roughly 30 times higher than the ambient ISM density. For the first time, optical emission is detected in the northwest area, beyond the open part of the radio shell. This detection of optical radiation along with other Hα and [SII] emitting structures in the south indicate an angular shock radius of 59′. Further X-ray observations would be needed to verify the correlation with the optical radiation in this area and to firmly establish the luminosity of the thermal component, thus further constraining the preshock ISM density and the explosion energy.

Acknowledgements. We would like to thank the referee, T. Landecker for his comments which helped to clarify certain issues of this work and N. D. Kylafis, J. Raymond and R. Smith for their useful suggestions. Skinakas Observatory is a collaborative project of the University of Crete, the Foundation for Research and Technology-Hellas and the Max-Planck-Institut für Extraterrestrische Physik. This work has been supported by a P.EN.E.D. program of the General Secretariat of Research and Technology of Greece. This research has made use of data obtained through the High Energy Astrophysics Science Archive Research Center Online Service, provided by the NASA/Goddard Space Flight Center.

References

Bisnovatyi-Kogan G.S., Silich S.A., 1995, Reviews of Modern Physics 67, 661

Blandford R.D., Cowie L.L., 1982, ApJ 260, 625
Condon J.J., Broderick J.J., Seielstad G.A., Douglas K., Gregory P.C., 1994 AJ 107, 1829
Cox D.P., 1972, ApJ 178, 143
Cox D.P., Raymond J.C., 1985, ApJ 298, 651
Dopita M.A., 1979, ApJS 40, 455
Fesen R.A., Kirshner R.P., 1980 ApJ 242, 1023
Fesen R.A., Blair W.P., Kirshner R.P., Gull T.R., Parker R.A.R., 1981, ApJ 247, 148
Fesen R.A., Gull T.R., Ketelsen D.A., 1983, ApJS 51, 337
Fesen R.A., Hurford A.P., 1995, AJ 110, 747
Hakkila J., Myers J.M., Stidham B.J., Hartmann D.H., 1997, AJ 114, 2043
Kaler J.B., 1976, ApJS 31, 517
Hester J.J., 1987, ApJ 314, 187
Hnatyk B., Petruk O., 1999, A&A 344, 295
Maciejewski W., Cox D.P., 1999, ApJ 511, 972
McKee C.F., Cowie L., 1975, ApJ 195, 715
Osterbrock D.E., 1989, Astrophysics of gaseous nebulae. W.H. Freeman & Company
Ostriker J.P., McKee C.F., 1988, Rev. Mod.Phys. 60, 1
Pineault S., Landecker T.L., Madore B., Gaumont-Guay S., 1993, AJ 105, 1060
Pineault S., Landecker T.L., Swerdlyk C.M., Reich W., 1997, A&A 324, 1152
Raymond J.C., Hester J.J., Cox.D., et al., 1988, ApJ 324, 869
Ryter C., Ceasarsky C.J., Audouze J., 1975, ApJ 198, 103
Seward F.D., Schmidt B., Slane P., 1995, ApJ 453, 284
Shelton R.L., Cox D.P., Maciejewski W., et al., 1998, astro-ph/9806090
Shaw R.A., Dufour R.J., 1995, PASP 107, 896
Sieber W., Salter C.J., Mayer C.J., 1981 A&A 103, 393
Slane P., Seward F.D., Bandiera R., Torii K., Tsumeni H., 1997, ApJ 485, 221
Wheelock S.L., Gautier T.N., Chillemi J., et al., 1994, IRAS sky survey atlas, Explanatory supplement
White R.L., Long K.S. 1991, ApJ 373, 543
Whitford A., 1958, AJ 63, 201